

International Journal of Modern Physics: Conference Series
 © World Scientific Publishing Company

TWO-PARTICLE CORRELATIONS IN pp AND Pb-Pb COLLISIONS WITH ALICE

XIANGRONG ZHU (for the ALICE Collaboration)

Key Laboratory of Quark & Lepton Physics (MOE) and Institute of Particle Physics, Central China Normal University, Wuhan 430079, China
E-mail: xiangrong.zhu@cern.ch

Received Day Month Year
 Revised Day Month Year

The measurement of azimuthal correlations between two particles is a powerful tool to investigate the properties of strongly-interacting nuclear matter created in ultra-relativistic heavy-ion collisions. We present measurements of di-hadron correlations in azimuth angle and pseudorapidity in Pb-Pb collisions at $\sqrt{s_{NN}} = 2.76$ TeV and photon-hadron correlations in pp collisions at $\sqrt{s} = 7$ TeV with the ALICE detector, respectively. In di-hadron correlations, the near-side jet shape in the short-range correlation region is quantitatively analyzed at $p_{T, \text{trig}} < 8$ GeV/c, and the modification of jet-particle yield, I_{AA} and I_{CP} , is measured at $8 < p_{T, \text{trig}} < 15$ GeV/c. In photon-hadron correlations, isolated leading photon and associated hadrons in its opposite azimuthal direction correlations are used to estimate the jet fragmentation function via the imbalance parameter, $x_E \equiv -\frac{\vec{p}_T^\gamma \cdot \vec{p}_T^{h\pm}}{|\vec{p}_T^\gamma|^2}$.

Keywords: ultra-relativistic heavy-ion collisions; two-particle correlations; medium effects; fragmentation function.

1. Introduction

The research objective of ultra-relativistic heavy-ion collisions is to explore the properties of the quark-gluon plasma (QGP), a deconfined state of quarks and gluons. Many experimental and theoretical studies of the QGP have been obtained from the study of hadron jets, the fragmentation products of high transverse momentum (p_T) partons^{1,2,2,3,4,5}. It is generally accepted that prior to hadronization, partons lose energy in the extreme hot and dense medium due to gluon radiation and multiple collisions. These phenomena are broadly known as “jet quenching”^{6,7,8}. At the LHC, the strong jet quenching in central heavy-ion collisions has been reported by ALICE, ATLAS and CMS collaborations^{9,10,11}. The nuclear suppression factor R_{AA} , which quantifies the suppression of charged hadrons, in central Pb-Pb collisions at $\sqrt{s_{NN}} = 2.76$ TeV is about 0.14 at $p_T \sim 7$ GeV/c^{9,11}. Furthermore, a strong di-jet energy asymmetry for leading jet transverse momenta above 100 GeV/c has been reported^{12,13}. At low transverse momenta ($p_{T, \text{jet}} < 50$ GeV/c), background fluctuations due to the underlying event dominate¹⁴ and event-by-event jet recon-

2 *X. Zhu (for the ALICE Collaboration)*

struction becomes difficult. Two-particle correlations allow the study of medium effects on the jet fragmentation without the need for jet reconstruction.

Especially, direct photon-hadron correlations offer two major advantages as compared to di-jet measurements because of the nature of the photon. First, in contrast to partons, photons do not carry color charge and hence do not interact strongly when traversing the medium¹⁵. Second, the direct photon production at leading order (LO) in pp and A+A collisions is dominated by the QCD compton scattering process, $q + g \rightarrow q + \gamma$ and $q + q \rightarrow g + \gamma$ annihilation process, and the photon momentum in the center-of-mass frame is exactly balanced by that of the recoil parton. For these reasons, direct photon-hadron correlations have been considered as a “golden channel” for studying the properties of parton energy loss including parton fragmentation function without the need of the jet reconstruction^{16,17}. Furthermore, significant measurements about parton energy loss in the medium by isolated photon-jet correlations at CMS are presented in¹⁸.

This proceeding is organized as follows: Sec. 2 briefly presents the ALICE detector relevant to this analysis and data sample. Sec. 3 shows the method of two-particle correlations. The near-side jet shape analysis is discussed in Sec. 3.1 and the modification factor of jet-particle yield is discussed in Sec. 3.2. Sec. 3.3 has the discussion of fragmentation function estimation from isolated photon-hadron correlations. Sec. 4 summarizes the results from this proceeding.

2. Detector and data sample

The analyzed data were taken with the ALICE detector described in detail in¹⁹. The collision vertex finding and tracking are performed using information from the Inner Tracking System (ITS) and the Time Projection Chamber (TPC). The ITS consists of six layers equipped with Silicon Pixel Detector (SPD), Silicon Drift Detector (SDD) and Silicon Strip Detector (SSD). The TPC is a cylindrical drift detector with uniform acceptance in azimuth angle (ϕ) and a pseudorapidity coverage of $|\eta| < 0.9$. The reconstructed vertex information is used to select primary track candidates and constrain the p_T of the track. The forward scintillators (VZERO) determine the centrality of the Pb-Pb collisions. Details can be found in²⁰. The photon is detected using the electromagnetic calorimeter (EMCal) which is a Pb-Scintillator sampling calorimeter covering $\Delta\phi = 100^\circ$ in the azimuthal angle and $|\eta| < 0.7$ in pseudorapidity. Photon candidates are selected from energy clusters deposited in the p_T range at 8 to 25 GeV/c by photon identification cuts. The photon identification cuts include track matching, cluster time and the cluster shower shape long axis parameter, λ_0^2 , defined as:

$$\lambda_0^2 = 0.5 \times (d_{\eta\eta} + d_{\phi\phi}) + \sqrt{0.25 \times (d_{\eta\eta} - d_{\phi\phi})^2 + d_{\eta\phi}^2} \quad (1)$$

where d_{ii} is the cluster position in i direction weighted by the cell energy.

In the di-hadron correlation analysis, about 14 millions minimum-bias Pb-Pb

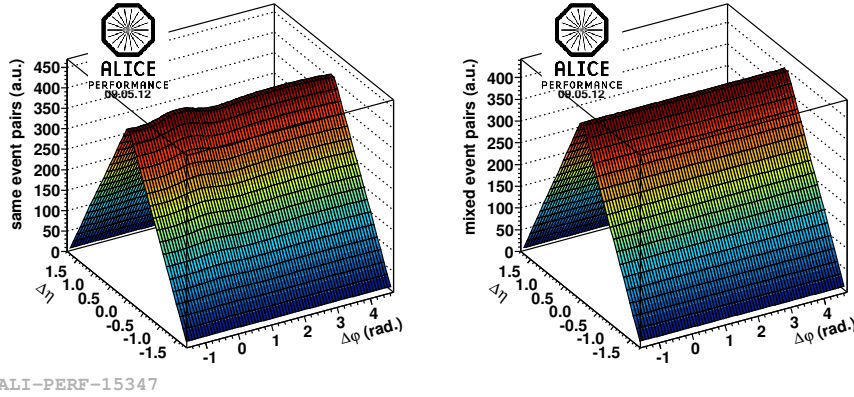


Fig. 1. Correlation constructed from pairs of particles from the same events (left panel) and the mixed events (middle panel)²¹.

collision events with an integrated luminosity (L_{int}) of $1.7 \mu\text{b}^{-1}$ at $\sqrt{s_{\text{NN}}} = 2.76 \text{ TeV}$ collected in fall 2010 and 37 millions pp events with the L_{int} of 6.8 nb^{-1} from March 2011 at $\sqrt{s} = 2.76 \text{ TeV}$ are used. In the isolated photon-hadron correlation analysis, 10 million pp events with the L_{int} of 500 nb^{-1} at $\sqrt{s} = 7 \text{ TeV}$ triggered by the EMCAL with a trigger threshold about $5 \text{ GeV}/c$ is used for achieving the measurement of high- p_{T} photons up to $25 \text{ GeV}/c$ with enough rate.

3. Correlation analysis

The p_{T} dependence of the correlation is studied by measuring triggered correlations. In such an analysis, a particle is chosen from a p_{T} region and called the *trigger particle*. The so called *associated particles* from another p_{T} region are correlated to the trigger particle where $p_{\text{T,assoc}} < p_{\text{T,trig}}$. The associated per-trigger yield is measured as a function of the azimuthal angle difference $\Delta\phi = \phi_{\text{trig}} - \phi_{\text{assoc}}$ and pseudorapidity difference $\Delta\eta = \eta_{\text{trig}} - \eta_{\text{assoc}}$:

$$Y(\Delta\phi, \Delta\eta) = \frac{1}{N_{\text{trig}}} \frac{dN_{\text{assoc}}}{d\Delta\phi d\Delta\eta} \quad (2)$$

where N_{assoc} is the number of particles associated to a number of trigger particles N_{trig} . This quantity is measured for different ranges of $p_{\text{T,trig}}$ and $p_{\text{T,assoc}}$.

To obtain the fully corrected per-trigger associated primary particle yield, two steps are performed on the raw correlations. Firstly, two-track efficiency and acceptance are assessed by using a mixed-event technique: the differential yield defined in Eq. 2 is also constructed for pairs where the trigger and the associated particle come from different events with similar centrality (or multiplicity in pp) and z -vertex position. The angular correlation constructed from particles within the same event

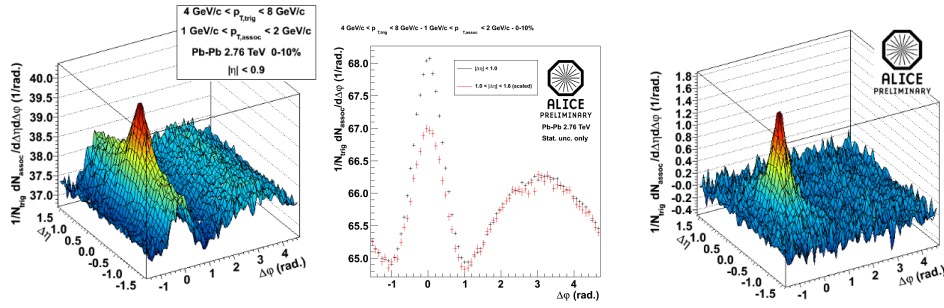
4 *X. Zhu (for the ALICE Collaboration)*


Fig. 2. Left: per-trigger yield; middle: per-trigger yield projection to $\Delta\phi$ in $1 < |\Delta\eta| < 1.6$ (red) and $|\Delta\eta| < 1$ (black); right: per-trigger yield subtracted flow contributions. Shown is at trigger $4 < p_{T, \text{trig}} < 8 \text{ GeV}/c$, associated $1 < p_{T, \text{assoc}} < 2 \text{ GeV}/c$ in most central Pb-Pb collisions²¹.

and mixed events are shown in the left and right panel in Fig. 1. The acceptance corrected distribution can be obtained from the ratio of pair distributions from the same and mixed events with a proper normalization factor. The normalization factor is chosen in a way which the distribution in mixed events is 1 at $\Delta\phi = \Delta\eta = 0$. Secondly, tracking efficiency and track contamination from secondary particles are used to correct the correlation function.

3.1. Near-side jet shape

A typical per-trigger yield is shown in the left panel of Fig. 2. At low p_T , per-trigger yield includes a sizable contribution from collective flow with a strong modulation in $\Delta\phi$ but independent of $\Delta\eta$. For isolating jet-like correlations to study the shape of the near-side jet peak, the flow contributions are determined in the long-range correlation region at $1 < |\Delta\eta| < 1.6$ and subtracted from the short-range correlation region at $|\Delta\eta| < 1$. This prescription called the η -gap method provides a measurement independent of the flow strength. The middle panel of Fig. 2 shows the projection to azimuthal $\Delta\phi$ in $1 < |\Delta\eta| < 1.6$ (red) and $|\Delta\eta| < 1$ (black). The difference between the two distributions in the near-side is the signal to be searched. The away-side peak is removed by construction in this procedure. Hence, the away-side region can not be studied with this method. The right panel of Fig. 2 shows the subtracted per-trigger yield distribution in $\Delta\phi$ and $\Delta\eta$ with $4 < p_{T, \text{trig}} < 8 \text{ GeV}/c$ and $1 < p_{T, \text{assoc}} < 2 \text{ GeV}/c$ in most central Pb-Pb collisions.

In order to quantify the near-side peak shape, the peak is fitted with a sum of two 2D Gaussians with the center at $\Delta\phi = \Delta\eta = 0$. The fit parameters are used to calculate the *rms* (equal to the square root of the variance, σ , for distributions centered at 0) in $\Delta\phi$ and $\Delta\eta$ direction ($\sigma_{\Delta\phi}$, $\sigma_{\Delta\eta}$). Fig. 3 presents the centrality dependence of $\sigma_{\Delta\phi}$ and $\sigma_{\Delta\eta}$ together with reference results from pp collisions in five different bins of $p_{T, \text{trig}}$ and $p_{T, \text{assoc}}$. The results indicate that the $\sigma_{\Delta\phi}$ is independent of centrality within the errors, and decreases with increasing $p_{T, \text{trig}}$ and $p_{T, \text{assoc}}$, whereas the $\sigma_{\Delta\eta}$ has a significant increase of moving from pp to central collisions

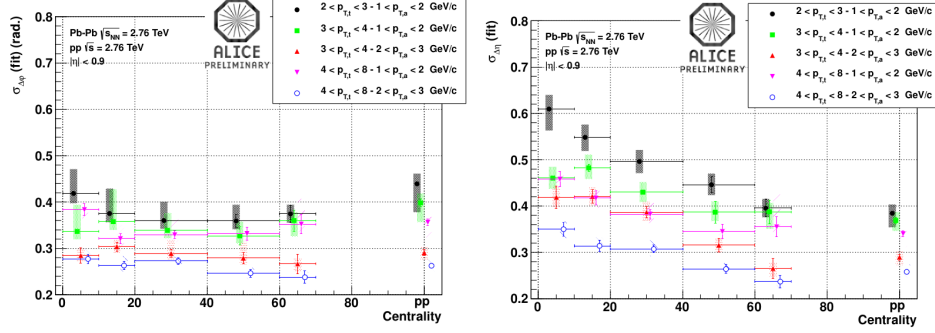


Fig. 3. Centrality dependence of $\sigma_{\Delta\phi}$ (left) and $\sigma_{\Delta\eta}$ (right) in five different $p_{T,\text{trig}}$ and $p_{T,\text{assoc}}$ p_T bins.

and also decreases with higher $p_{T,\text{trig}}$ and $p_{T,\text{assoc}}$. More details about this analysis can be found in^{21,22}.

3.2. Modification of the jet-particle yield

At higher p_T ($p_{T,\text{trig}} > 8$ GeV/c, $p_{T,\text{assoc}} > 3$ GeV/c) where collective effects are small and jet-like correlations dominate, the medium modification of the jet-particle yield has been studied by calculating ratios of yields on the near-side and away-side. In order to remove uncorrelated background from the yield, a pedestal value is determined by a constant fitting the region close to the minimum of the $\Delta\phi$ distribution ($\Delta\phi \approx \pm\pi/2$) where uncorrelated background is dominated. A background shape considering the elliptic flow parameter v_2 is also analyzed. For a given p_T bin, the v_2 background is calculated as $2\langle v_{2,\text{trig}} \rangle \langle v_{2,\text{assoc}} \rangle \cos 2\Delta\phi$. The v_2 values are taken from an independent measurement²³. The η -gap method, described in Sec. 3.1, is also used to remove the contributions from $\Delta\eta$ -independent correlations on the near-side of the per-trigger yield. Subsequent to the background subtraction, the near-side and away-side yields are integrated within $|\Delta\phi| < 0.7$ and $|\Delta\phi \pm \pi| < 0.7$, respectively.

The modification of the jet-particle yield is calculated by the ratio of the per-trigger yield in Pb-Pb to pp collisions (I_{AA}) and the yield in central to peripheral in Pb-Pb collisions (I_{CP}) with $I_{AA} = Y_{\text{Pb-Pb}}/Y_{\text{pp}}$ and $I_{CP} = Y_{\text{central}}^{\text{Pb-Pb}}/Y_{\text{peripheral}}^{\text{Pb-Pb}}$, respectively. The top panel in Fig. 4 presents the yield modification factor I_{AA} for central and peripheral Pb-Pb collisions using the three background subtraction schemes as discussed. The main significant difference is in the lowest $p_{T,\text{assoc}}$ interval that confirms the small bias due to flow anisotropies in this p_T region. In central collisions, an away-side suppression from in-medium energy loss is observed ($I_{AA} \approx 0.6$). Moreover, there is an enhancement above unity of ($I_{AA} \approx 1.2$) on the near-side which has not been observed with any significance at lower collision energies²⁶. In peripheral collisions, both near-side and away-side are consistent with unity.

Furthermore, the bottom panel in Fig. 4 shows the ratio of the yield in central

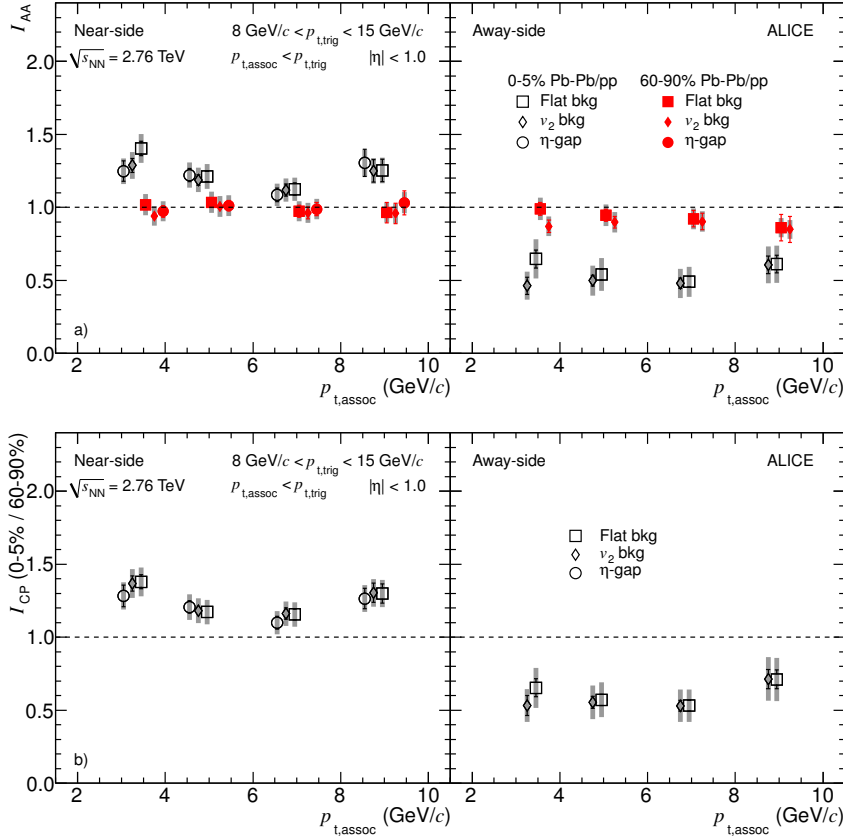
6 *X. Zhu (for the ALICE Collaboration)*


Fig. 4. I_{AA} (top panel) for central (open black symbols) and peripheral (filled red symbols) collisions, and I_{CP} (bottom panel). Different background subtraction schemes, a flat pedestal (squares), v_2 subtraction (diamonds) and η -gap subtraction (circles, only near-side) are presented^{24,25}.

and peripheral collisions, I_{CP} . The result of I_{CP} is consistent with I_{AA} in central collisions with respect to the near-side enhancement and the away-side suppression.

A significant near-side enhancement of I_{AA} and I_{CP} in the p_T region observed shows that the near-side parton is also subject to medium effects. I_{AA} is sensitive to (i) a change of the fragmentation function, (ii) a possible change of the quark/gluon jet ratio in the final state due to the different coupling to the medium, and (iii) a bias on the parton p_T spectrum after energy loss due to the trigger particle selection. More details about this analysis can be found in^{24,25}.

3.3. Fragmentation function

In isolated photon-hadron correlations, the away-side distribution provides a measurement of the full fragmentation function of the jet at the opposite azimuthal

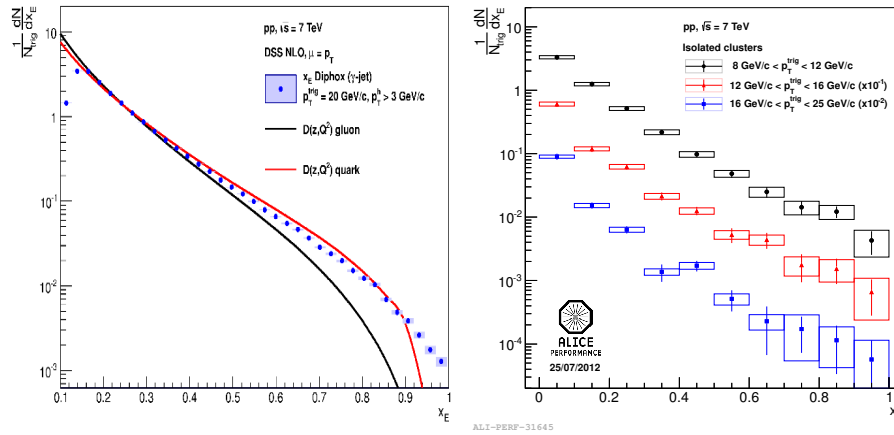


Fig. 5. Left: x_E distribution from γ -jet production produced by Diphox, and compared to DSS quark and gluon fragmentation; right: x_E distribution of isolated cluster (photon candidate)-hadron correlations in three $p_{T, \text{trig}}$ bins³⁰.

direction of the isolated photon. In leading order pQCD, the fragmentation function of the recoil jet from the away-side parton should be given to a good approximation by the imbalance parameter x_E distribution as:

$$x_E = -\frac{\vec{p}_T^\gamma \cdot \vec{p}_T^{h^\pm}}{|\vec{p}_T^\gamma|^2} = -\frac{|p_T^{h^\pm}| \cos \Delta\phi}{|p_T^\gamma|} \quad (3)$$

where $\Delta\phi$ is the azimuthal angle between isolated photons and hadrons. The transverse and longitudinal momenta of away-side parton does not exactly balance with the isolated photon. Hence, the parameter x_E is an approximation rather than an exact measurement to the fragmentation function of the away-side jet²⁷. This analysis is only performed with pp collisions at $\sqrt{s} = 7 \text{ TeV}$. The left panel in Fig. 5 shows the x_E distribution computed from Diphox γ -jet production²⁸ and comparison with DSS quark and gluon fragmentation function²⁹. It indicates that the x_E distribution mainly follows the quark fragmentation behaviour in a large range (0.2 to 0.8) because of the dominant contribution of compton scattering process.

Clusters filtered by EMCAL photon identification cuts, photon candidates, are dominated by a large fraction of decay photons of neutral mesons (mostly π^0). The fraction is reduced about 80% by applied isolation criteria. In this analysis, the isolation criteria requires no particles including charged and neutral particles with $p_T > 0.5 \text{ GeV}/c$ in a cone of radius $R = \sqrt{\Delta\phi^2 + \Delta\eta^2} = 0.4$ around a photon candidate with largest p_T in one event. The right panel in Fig. 5 presents the x_E distribution from isolated cluster (photon candidate)-hadron correlations with isolated leading cluster p_T at $8 < p_{T, \text{trig}} < 12 \text{ GeV}/c$ (black), $12 < p_{T, \text{trig}} < 16 \text{ GeV}/c$ (red), and $16 < p_{T, \text{trig}} < 25 \text{ GeV}/c$ (blue). Two decay photons from high p_T π^0 are generally close and their two electromagnetic showers overlapping in

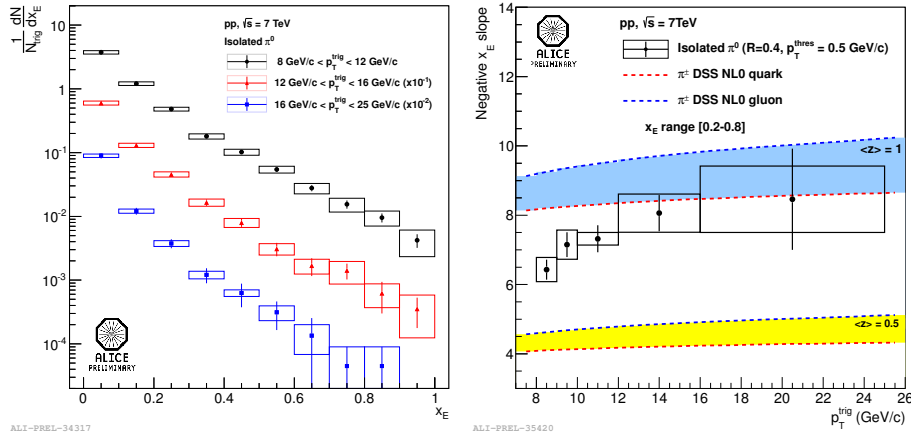
8 *X. Zhu (for the ALICE Collaboration)*


Fig. 6. Left: x_E distributions of isolated π^0 -hadron correlations in three $p_{T, \text{trig}}$ bins; right: slopes extracted from exponential fit of isolated π^0 -hadron correlations and compared to DSS quark-gluons fragmentation functions³⁰.

the calorimeter cells are clustered. A fraction of the clusters rejected unsuccessfully by photon identification cuts are the dominant contamination of isolated photons. In order to subtract the contamination, the x_E distribution of isolated π^0 -hadron correlations is measured, see the left panel in Fig. 6. Compared to inclusive π^0 , the isolated π^0 equally carries a large fraction of its parent parton energy from 0.5 to 0.8. An exponential slope is extracted from fitting the x_E distribution of isolated π^0 -hadron correlations and compared to DSS fragmentation functions shown in the right panel in Fig. 6. The comparison indicates that the isolated π^0 is a parton fragmentation product and $p_T^{\pi^0} < p_T^{\text{parton}}$.

To subtract the contamination contribution to the x_E distribution, the isolated photon purity is estimated firstly by two-component binned likelihood method: a mix of scaled signal and contamination distribution is used to fit all clusters in pp collision data at shower shape long axis λ_0^2 distribution, see the left panel in Fig. 7. Here, the signal component is obtained from γ -jet events generated with PYTHIA and propagated through the detectors with GEANT3, and the contamination component is extracted from data by selecting events which have failed the isolation criteria. The typical purity values obtained from this method in $8 < p_T < 25 \text{ GeV}/c$ increase from about 5% to 70%. The x_E distribution of isolated π^0 -hadron correlations scaled with respect to the isolated photon purity estimated previous is subtracted from isolated cluster-hadron correlations. In the meanwhile, the underlying events x_E contributions which are estimated at two different regions $\frac{\pi}{3} < \Delta\phi < \frac{2\pi}{3}$ and $\frac{4\pi}{3} < \Delta\phi < \frac{5\pi}{3}$ are also removed from the isolated cluster-hadron correlations. The x_E distribution of isolated photon-hadron correlations is shown in the right panel in Fig. 7, and a slope 7.8 ± 0.9 is obtained from the fitting of x_E distribution at $0.2 < x_E < 0.8$. More details about this analysis can be found in³⁰.

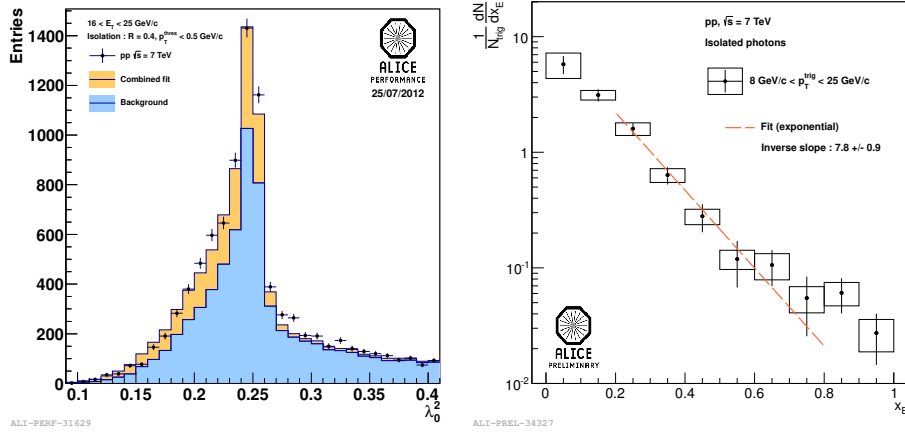


Fig. 7. Left: isolated cluster shower shape long axis λ_0^2 distribution fitted by a two-component binned likelihood; right: x_E distributions of isolated photon-hadron correlations at $8 < p_T^{\text{iso}} < 25 \text{ GeV}/c$ ³⁰.

4. Summary

Two-particle correlations have been used to study the properties of the hot and dense medium with ALICE at LHC. In di-hadron correlations, the medium effect on the near-side jet peak is quantified at transverse momenta below $10 \text{ GeV}/c$. A broadening at lower p_T intervals of trigger and associated particles and in more central Pb-Pb collisions is observed. The near-side peaks show a significant increase in $\Delta\eta$ moving from pp to central Pb-Pb collisions and no centrality dependence in $\Delta\phi$ within errors. This might be an indication of interaction of jets with longitudinal flow. At higher p_T , the modification factors I_{AA} and I_{CP} of the jet-particle yield show a strong suppression on the away-side consistent with strong medium energy loss as well as an interesting near-side enhancement by effect of medium at the LHC. The fragmentation function in pp collisions is calculated by the imbalance parameter x_E extracted from isolated leading photon-hadron correlations.

5. Acknowledgement

This work is partly supported by the “973” Grant of MOST of China 2013CB837803, the NSFC Key Grant 11020101060, IRG11221504, 11375071, 11005044, the CCNU Key Grant CCNU13F026 and QLPL2012P01.

References

1. D. d’Enterria, in *Nuclei-Relativistic Heavy Ion Physics*, Landolt-Bornstein, Group I, Vol. 23 (Springer-Verlag, Berlin, 2010).
2. BRAHMS Collab. (I. Arsene *et al.*), *Nucl. Phys. A* **757**, 1 (2005).
3. PHENIX Collab. (K. Adcox *et al.*), *Nucl. Phys. A* **757**, 184 (2005).
4. PHOBOS Collab. (B. B. Back *et al.*), *Nucl. Phys. A* **757**, 28 (2005).

10 X. Zhu (for the ALICE Collaboration)

5. STAR Collab. (J. Adams *et al.*), *Nucl. Phys. A* **757**, 102 (2005).
6. J. D. Bjorken, *FERMILAB-PUB-82-059-THY* (1982).
7. M. Gyulassy and M. Plumer, *Phys. Lett. B* **243**, 432 (1990).
8. X.-N. Wang and M. Gyulassy, *Phys. Rev. Lett.* **68**, 1480 (1992).
9. ALICE Collab. (K. Aamodt *et al.*), *Phys. Lett. B* **696**, 30 (2011).
10. ATLAS Collab. (G. Aad *et al.*), *Phys. Lett. B* **719**, 220 (2013).
11. CMS Collab. (S. Chatrchyan *et al.*), *Eur. Phys. J. C* **72**, 1945 (2012).
12. ATLAS Collab. (G. Aad *et al.*), *Phys. Rev. Lett.* **105**, 252303 (2010).
13. CMS Collab. (S. Chatrchyan *et al.*), *Phys. Rev. C* **84**, 024906 (2011).
14. ALICE Collab. (B. Abelev *et al.*), *JHEP* **03**, 053 (2012).
15. PHENIX Collab. (S. S. Adler *et al.*), *Phys. Rev. Lett.* **94**, 232301 (2005).
16. X.-N. Wang and Z. Huang, *Phys. Rev. C* **55**, 3047 (1997).
17. X.-N. Wang, Z. Huang and I. Sarcevic, *Phys. Rev. Lett.* **77**, 231 (1996).
18. CMS Collab. (S. Chatrchyan *et al.*), *Physics Letters B* **718**, 733 (2013).
19. ALICE Collab. (K. Aamodt *et al.*), *JINST* **3**, S08002 (2008).
20. ALICE Collab. (K. Aamodt *et al.*), *Phys. Rev. Lett.* **106**, 032301 (2011).
21. J. F. Grosse-Oetringhaus (for the ALICE Collaboration), *Nuclear Physics A* **910**, 58 (2013).
22. A. Morsch (for the ALICE Collaboration), *Nuclear Physics A* **910**, 281 (2013).
23. ALICE Collab. (K. Aamodt *et al.*), *Phys. Rev. Lett.* **107**, 032301 (2011).
24. ALICE Collab. (K. Aamodt *et al.*), *Phys. Rev. Lett.* **108**, 092301 (2012).
25. J. F. Grosse-Oetringhaus (for the ALICE Collaboration), *J. Phys. G: Nucl. Part. Phys.* **38**, 124028 (2011).
26. STAR Collab. (J. Adams *et al.*), *Phys. Rev. Lett.* **97**, 162301 (2006).
27. PHENIX Collab. (A. Adare *et al.*), *Phys. Rev. C* **80**, 024908 (2009).
28. T. Binnoth, J. P. Guillet, E. Pilon and M. Werlen, *Eur. Phys. J. C* **16**, 311 (2000).
29. D. de Florian, R. Sassot and M. Stratmann, *Phys. Rev. D* **75**, 114010 (2007); *Phys. Rev. D* **76**, 074033 (2007).
30. N. Arbor (for the ALICE Collaboration), *Nuclear Physics A* **904**, 697c (2013).